



PCCP

**Identifying the Acceptor State in NiO Hole Collection Layers:
Direct Observation of Exciton Dissociation and Interfacial
Hole Transfer Across a Fe₂O₃/NiO Heterojunction**

Journal:	<i>Physical Chemistry Chemical Physics</i>
Manuscript ID	CP-COM-07-2018-004502.R1
Article Type:	Paper
Date Submitted by the Author:	30-Aug-2018
Complete List of Authors:	Biswas, Somnath; The Ohio State University, Chemistry and Biochemistry Husek, Jakub; The Ohio State University, Chemistry and Biochemistry Londo, Stephen; The Ohio State University, Chemistry and Biochemistry Fugate, Elizabeth; The Ohio State University, Chemistry and Biochemistry Baker, Lawrence; Ohio State University, Chemistry and Biochemistry

SCHOLARONE™
Manuscripts

Cite this: DOI: 10.1039/xxxxxxxxxx

Identifying the Acceptor State in NiO Hole Collection Layers: Direct Observation of Exciton Dissociation and Interfacial Hole Transfer Across a Fe₂O₃/NiO Heterojunction[†]

Somnath Biswas, Jakub Husek, Stephen Londo, Elizabeth A. Fugate, and L. Robert Baker*

Received Date
Accepted Date

DOI: 10.1039/xxxxxxxxxx

www.rsc.org/journalname

NiO is widely utilized as a hole transport layer in solar energy devices where light absorption in a photoactive layer is followed by charge separation and hole injection into a NiO collection layer. Due to the complex electronic structure of the hybridized valence band in NiO, the chemical nature of the hole acceptor state has remained an open question, despite the fact that hole localization in this material significantly influences device efficiency. To comment on this, we present results of ultrafast charge carrier dynamics in a NiO based model heterojunction (Fe₂O₃/NiO) using extreme ultraviolet reflection-absorption (XUV-RA) spectroscopy. Element specific XUV-RA spectroscopy demonstrates the formation of transient Ni³⁺ within 10 ps following selective photoexcitation of the underlying Fe₂O₃ substrate. This indicates that hole transfer in this system occurs to NiO valence band states composed of significant Ni 3d character. Additionally, we show that this hole injection process proceeds via a two-step sequential mechanism where fast, field-driven exciton dissociation occurs in Fe₂O₃ in 680 ± 60 fs, followed by subsequent hole injection to NiO in 9.2 ± 2.9 ps. These results reveal the chemical nature of the hole acceptor state in widely used NiO hole transport layers and provides a direct observation of exciton dissociation and interfacial hole transfer in this model system.

1 Introduction

The use of hole transport layers in solar materials is an essential architectural element that enables efficient energy harvesting by solid-state devices.^{1–5} In particular, nickel oxide (NiO) has been extensively used as a hole transport layer due to its wide band gap, suitable valence band alignment with multiple photosensitizers, high p-type conductivity, and chemical stability.^{3,6–8} The kinetics of interfacial hole transfer from a photosensitizer to a NiO layer and the electronic structure of the hole acceptor state in NiO are known to strongly influence overall device efficiency.^{1,9–11} However, the details of this process are not yet entirely understood due to the challenges associated with direct, real-time observation of carrier dynamics at interfaces.

The kinetics of field-driven exciton dissociation influences the quantum efficiency of light harvesting devices where charge sep-

aration competes with recombination dynamics.^{12,13} A number of approaches have been used to calculate or estimate the rate of exciton dissociation and interfacial charge injection; however, the ability to independently resolve exciton dissociation and charge transfer in real-time with chemical state resolution would provide critical insight regarding the interfacial electronic structure that mediates charge separation and energy conversion efficiency.^{13–16} Charge separation at semiconductor heterojunctions can occur by two possible mechanisms. In a first case it is possible that the interfacial electric field in the space charge region is sufficiently strong to drive exciton dissociation, and charge transfer occurs by subsequent drift of the minority carrier across the interface.¹⁷ In a second case it is possible that the exciton remains bound in the depletion region and that charge separation only occurs upon exciton arrival at a type II interface where the difference in electron affinities between the donor and acceptor levels drive exciton dissociation.¹⁸ These two cases are depicted schematically in Figure 1 for a model heterojunction Fe₂O₃/NiO. Energy levels in Figure 1 are drawn to scale, where the band gaps (NiO: 3.6 eV, Fe₂O₃: 2.1 eV), Fermi levels (NiO: 5 eV, Fe₂O₃: 4.39 eV), valence band of NiO (5.5 eV) and conduction band of Fe₂O₃

The Ohio State University, Department of Chemistry and biochemistry, Columbus, OH, 43210, USA, Tel: (+1)614 - 292 - 2088

* Corresponding author; E-mail: baker.2364@osu.edu

† Electronic Supplementary Information (ESI) available: [details of any supplementary information available should be included here]. See DOI: 10.1039/cXCP00000x/

(4.09 eV) are adapted from previous results.^{19–22}

To experimentally differentiate between case 1 and case 2 kinetics requires the ability to spectroscopically resolve exciton dissociation and interfacial charge transfer separately. Specifically, case 1 would follow a sequential two-step kinetic rate equation where exciton dissociation precedes interfacial charge transfer, giving rise to three distinct states evolving sequentially in the time domain, namely a bound exciton state, a dissociated state, and an interfacial charge transfer state. Alternatively, case 2 would follow a single step rate equation where exciton dissociation and interfacial charge transfer occur as a single concerted process giving rise to only a bound exciton state and an interfacial charge transfer state.

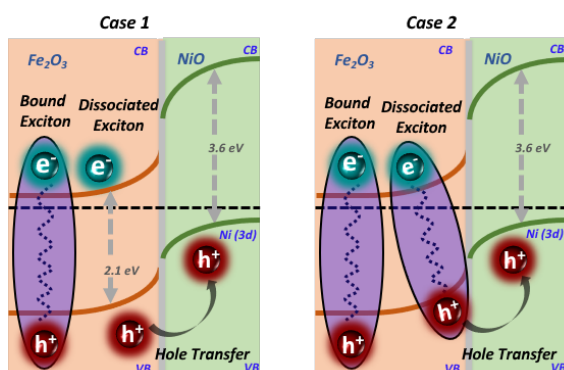


Fig. 1 Case 1 depicts a two-step sequential mechanism of hole transfer. The interfacial field drives the exciton dissociation in the space charge region of $\text{Fe}_2\text{O}_3/\text{NiO}$ heterojunction. The subsequent hole transfer occurs via the drift of the carrier across the interface. Case 2 depicts that the exciton remains bound in the depletion region, the bound exciton dissociates at the interface upon hole transfer.

X-ray spectroscopy is element and oxidation-state specific and accordingly offers the unique ability to track charge dynamics on both sides of a heterojunction by measuring the time evolution of element-specific absorption features that are unique to either side of the interface.^{23,24} Unfortunately, real-time observation of interfacial charge transfer by transient x-ray absorption spectroscopy are not readily achieved due to the relatively long pulse durations (~ 100 ps) achievable by synchrotron radiation, which precludes ultrafast measurement of electron motion at interfaces.^{25–28} A number of recent studies have demonstrated that ultrafast, tabletop extreme ultraviolet (XUV) light sources based on high harmonic generation can extend the benefits of x-ray absorption spectroscopy to the femtosecond (or even attosecond) time domain for the study of real-time electron dynamics with element-specific resolution.^{29–33}

In this study we employ element and oxidation state specific XUV-RA spectroscopy to study interfacial charge transfer and exciton dissociation dynamics in model $\text{Fe}_2\text{O}_3/\text{NiO}$ type II heterojunctions. XUV-RA was recently adapted by our group as a surface specific analog to XUV absorption spectroscopy to probe surface carrier dynamics with femtosecond time resolution.^{34–38} XUV reflectivity has also been recently used to study carrier relaxation dynamics in single-crystalline germanium.³⁹

We have selected $\text{Fe}_2\text{O}_3/\text{NiO}$ as a model heterojunction because NiO is a promising candidate to serve as a hole transport layer. NiO is already extensively utilized as a hole collection layer in dye sensitized solar cells,^{40,41} organic-inorganic hybrid perovskite solar cells,^{3,5} organic light-emitting diodes,^{2,4} and photovoltaics.¹ Despite the widespread applications of NiO, the valence band electronic structure as well as the mechanism of the hole transport in this material are not completely understood. Of particular interest is the chemical nature of the hole acceptor state in the valence band of NiO.

In many cases charge transfer to a metal containing complex is accounted for by assuming a unit oxidation state change in the metal center,^{42,43} leaving the question of where charge actually localizes between the metal d states and a potentially non-innocent ligand ambiguous. For example, using this nomenclature it could always be concluded that hole transfer from a light absorbing layer to NiO leads to the formation of transient Ni^{3+} . However, this approach fails to specify whether hole injection actually occurs to Ni 3d or O 2p valence band states. It has recently been noted that the chemical reactivity of nickel oxide depends greatly on the actual site of hole localization.⁴⁴

The valence band electronic structure in NiO is a subject of long-standing interest, and NiO has been separately described as both a charge-transfer as well as a Mott-Hubbard semiconductor.^{45,46} In a charge-transfer semiconductor the valence band maximum is mainly composed of O 2p states, while in a Mott-Hubbard semiconductor the valence band maximum is primarily composed of metal 3d states. The electronic structure of the hybridized valence band in NiO is further complicated by considering the presence of surface mid-gap states that are unavoidably associated with interfacial defects in NiO-based solar materials.^{47,48} Given the complex electronic structure of the valence band, the state specific determination of the hole acceptor state in NiO has remained an important challenge.

2 Materials and Methods

2.1 Preparation of thin films of Fe_2O_3 , NiO, and $\text{Fe}_2\text{O}_3/\text{NiO}$

Pure Fe_2O_3 and NiO samples were prepared by first sputtering the metal precursor onto a SiO_2 thermal oxide (100) wafer using a Kurt J. Lesker Co. Lab 18 Thin Film Deposition System. The thickness of the deposited metal film was monitored in situ using a quartz crystal microbalance (iron: DC sputtering at $0.6 \text{ \AA}/\text{sec}$ for 30 minutes; nickel: DC sputtering at $1.0 \text{ \AA}/\text{sec}$ for 15 minutes). Following metal deposition, the iron metal film was annealed in air at 520°C for 30 minutes to produce Fe_2O_3 , and nickel metal film was annealed in air at 500°C for 120 minutes to produce NiO.

To prepare $\text{Fe}_2\text{O}_3/\text{NiO}$ heterojunction samples, an AJA Orion DC Sputter Deposition tool was used to deposit the NiO overlayer onto previously prepared Fe_2O_3 . This was accomplished by depositing Ni metal in the presence of O_2 using an Ar flow rate of 20 sccm and an O_2 flow rate of 5 sccm. These deposition conditions are similar to those given in a work by Miller and Rocheleau.⁴⁹ The deposition rate of NiO was calculated by depositing under these conditions for five minutes. The resulting step edge

was measured to be 50 nm by AFM, yielding a deposition rate of 1.77 Å/sec for NiO. Heterojunctions of NiO on Fe₂O₃ were produced with the following NiO overlayer thicknesses: 2 nm, 3 nm, 5 nm, and 10 nm. Based on the measured rate, the required deposition time for these overlayers was 12, 18, 30, and 60 seconds, respectively. Ground state XUV-RA spectra for each of these heterojunction samples relative to pure Fe₂O₃ and NiO is provided as Figure S1 in the Supporting Information. All transient spectra reported here were collected from Fe₂O₃/NiO heterojunction samples having an average thickness of 5 nm. This thickness represents a good experimental choice for transient measurements because the NiO film is sufficiently thin to enable measurement of exciton dynamics in the Fe₂O₃ substrate but is sufficiently thick to resemble nearly defect-free NiO as described in detail in the Supporting Information. Additional characterization of the samples by SEM (Figure S3) and AFM (Figure S4) is also included in the Supporting Information.

2.2 XUV-RA Spectroscopy

Both static and transient XUV-RA measurements were performed under ultrahigh vacuum ($\sim 10^{-9}$ Torr). Experimental details have been described in our previous contributions.^{34,36} To summarize here, high harmonic XUV probe pulses are generated by focusing 2.0 mJ of 800 nm light into a semi-infinite gas cell (SIGC) filled with neon gas. This process generates odd harmonics of 800 nm (1.55 eV). Because centrosymmetric environments prohibit the generation of even order harmonics, an additional symmetry breaking field of 40 mJ pulse at 400 nm is overlapped with the 800 nm driving field in the gas interaction region, allowing the generation of both even and odd harmonics. An Al filter (0.6 μ m, Lebow) is used to remove residual 800 nm and 400 nm light from the XUV beam. A toroidal mirror is used to focus the XUV beam onto the sample at an incidence angle of 8° relative to the sample surface. The XUV beam reflected from the sample is subsequently spectrally dispersed onto a CCD detector (Andor, DO920P-BN) using an aberration corrected concave variable line spaced grating.

Fe₂O₃ and Fe₂O₃/NiO heterojunction samples were excited using a pump fluence of 6.3 mJ/pulse-cm² centered at a wavelength of 400 nm (area = 2.34 mm²). The 400 nm pump beam was produced by second harmonic generation from 2.9 W, 35 fs, 800 nm pulse. NiO was excited using a pump fluence of 5.3 mJ/pulse-cm² centered at a wavelength of 267 nm (area = 1.23 mm²). This pump beam was produced by third harmonic generation from the 800 nm pulse. The angle of incidence was 20° relative to the sample surface for both 400 nm and 267 nm pump beams. For time-resolved measurements, the XUV flux reflected from the sample is measured with both the optical pump beam on and off as a function of time delay between pump and probe pulses.

The time delay between pump and probe beams is controlled using a retroreflector and a linear delay stage (Newport, ILS150CC) with ≥ 1 μ m bidirectional repeatability. An Al filter (0.2 μ m, Lebow) is installed just before the detector to completely remove any pump beam scatter from the measured XUV reflectance spectrum. To avoid beam damage, the sample is rastered during data collection. The transient data reported in

Figure 2A–D represents the results of 9.8 hr, 7 hr, 8.7 hr, and 2.3 hr of total data integration for Fe₂O₃ pumped at 400 nm, NiO pumped at 267 nm, Fe₂O₃/NiO heterojunction pumped at 400 nm, and NiO pumped at 400 nm, respectively. All experimental spectra were frequency filtered using a bandstop filter between 0.5 and 0.79 eV⁻¹ to remove periodic oscillations resulting from spatial variation in the high harmonic probe pulse as described previously.³⁷

3 Results and Discussion

Because NiO has a wide band gap of 3.6 eV compared to the relatively small band gap (2.1 eV) of Fe₂O₃, it is possible to selectively photoexcite the Fe₂O₃ substrate and measure the transient response at the Fe and Ni M_{2,3}-edges independently. As previously reported, these element-specific resonances appear in the ranges of 52–56 eV and 62–70 eV for Fe and Ni, respectively.³⁷ We have also investigated the dynamics in pure Fe₂O₃ and pure NiO for comparison. Ground state XUV-RA spectra of pure Fe₂O₃, pure NiO, and the Fe₂O₃/NiO heterojunction showing the expected element specific M_{2,3}-edge resonances of Fe and Ni are provided in the Supporting Information (see Figure S1).

Figure 2 shows contour plots depicting the time evolution of transient signal at the Fe and Ni M_{2,3}-edges for pure Fe₂O₃ (A), pure NiO (B), and the Fe₂O₃/NiO heterojunction (C). Because NiO has a wide band gap of 3.6 eV, Figure 2B represents dynamics induced by a 267 nm pump (4.7 eV) pulse, while Figure 2A and 2C represent results from a 400 nm (3.1 eV) pump pulse designed to selectively excite Fe₂O₃. As a control, NiO transient dynamics were also measured using a 400 nm pump, and the results are shown in Figure 2D.

In core-hole spectroscopy an increase in the oxidation state of a metal center induces a blue shift of the element specific absorption line while a decrease in oxidation state induces a red shift. This provides an accurate qualitative understanding of the transient spectra described below. For example, it has been previously shown that direct photoexcitation of Fe₂O₃ at 400 nm excites a charge transfer bandgap transition, where an electron is promoted from the primarily O 2p valence band states to the Fe 3d conduction band states.^{34,50,51} This results in a reduction of Fe³⁺ metal centers to Fe²⁺, which can be observed spectrally as a ground state bleach (GSB) of Fe³⁺ absorption at 55 eV and excited state absorption (ESA) by transient Fe²⁺ at 52.2 eV. A similar spectral response is observed at the Ni M_{2,3}-edge for NiO photoexcited at 267 nm, where GSB at 65.2 eV and 69.2 eV represents depletion of ground state Ni²⁺ population and ESA at 63.2 eV represents the formation of transient Ni⁺ also consistent with a charge transfer band gap excitation. These qualitative assignments have been verified previously for Fe₂O₃^{34,50} and NiO³⁷ using semi-empirical spectral simulations based on ligand field multiplet calculations.

Comparison of Figures 2A and 2C shows two differences between the transient kinetics of Fe₂O₃ (A) compared to the Fe₂O₃/NiO heterojunction (C) following photoexcitation with 400 nm light. First, we observe that the Ni M_{2,3}-edge shows no transient response as expected for pure Fe₂O₃. In contrast the heterojunction sample shows a clear spectral signature at the Ni

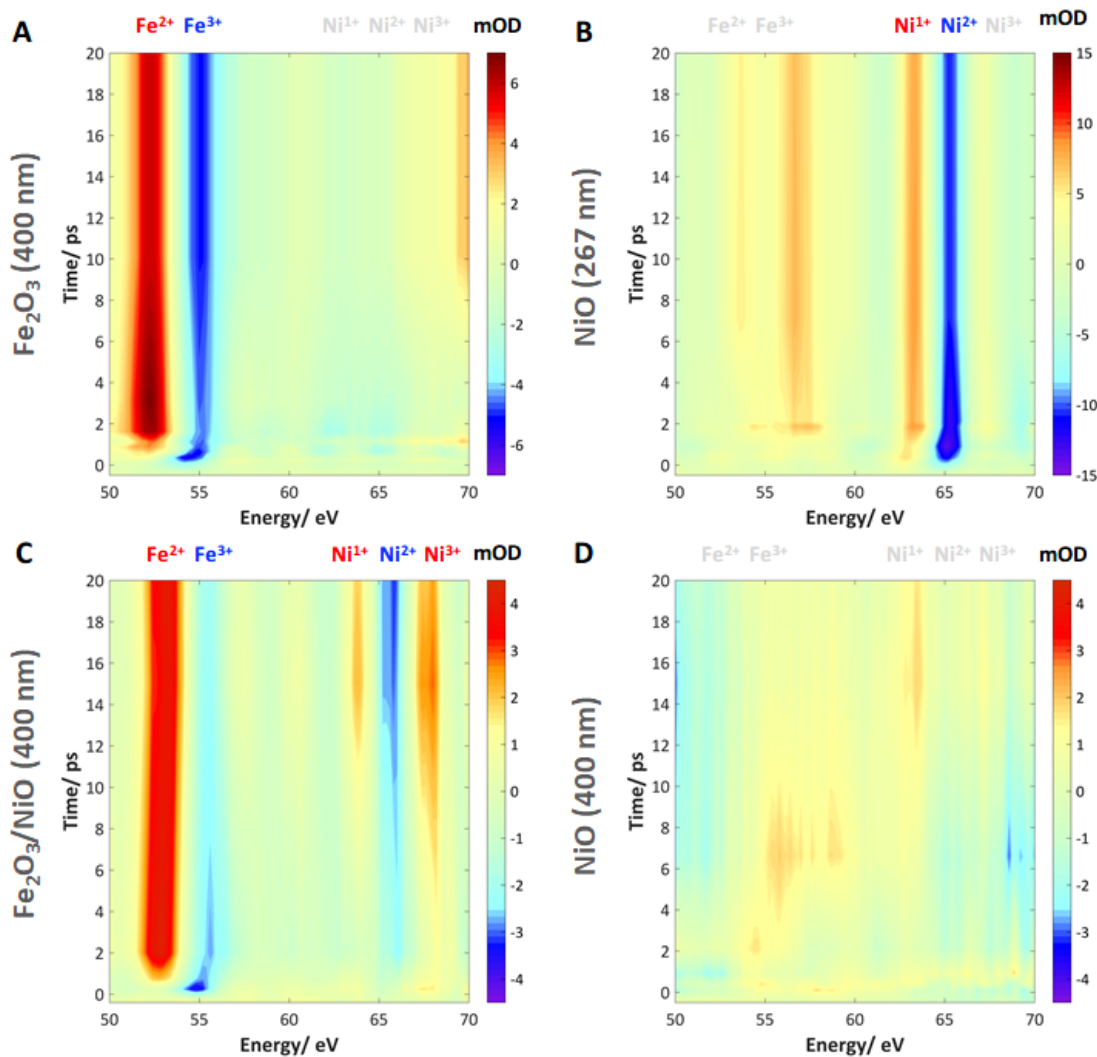


Fig. 2 (A, B) Contour plots showing the experimental transient reflection-absorption data of pure Fe_2O_3 (A) and pure NiO (B) pumped at 400 nm and 267 nm, respectively. (C, D) Contour plots showing the experimental transient reflection-absorption data of $\text{Fe}_2\text{O}_3/\text{NiO}$ heterojunction pumped at 400 nm (C) and pure NiO pumped at 400 nm (D). Associated spectra to each of these contour plot are provided in the Supporting Information.

$M_{2,3}$ -edge, which is delayed in time relative to the Fe $M_{2,3}$ -edge signal. Second, we observe that the transient signal at the Fe $M_{2,3}$ -edge, which initially appears identical between these two samples evolves quite differently for the case of the heterojunction sample compared to pure Fe_2O_3 . We first qualitatively assign the origin of these two spectral differences prior to performing a rigorous kinetic analysis of the associated data.

Signal at the Ni $M_{2,3}$ -edge measured for the $\text{Fe}_2\text{O}_3/\text{NiO}$ heterojunction sample consists of a GSB at 65.2 eV indicating a loss of Ni^{2+} population as well as an ESA at 68 eV indicating the formation of transient Ni^{3+} . We also observe a weak bleach at 69.2 eV consistent with the ground state doublet of Ni^{2+} (see Figure S1). However, because this feature is weaker than the GSB at 65.2 eV and slightly overlaps with ESA of the Ni^{3+} state, we take the 65.2 eV bleach as the primary marker for ground state depletion. The appearance of the Ni^{2+} GSB and Ni^{3+} ESA is correlated in time and measurably delayed relative to signal at the Fe $M_{2,3}$ -edge. For comparison, Figures 2B and 2D show the result of direct photoexcitation of pure NiO at 267 nm and 400 nm, respectively. For

267 nm excitation a clear spectral response is immediately visible at the Ni $M_{2,3}$ -edge within the 120 fs instrument response function. In contrast, no transient response is observed within noise for photoexcitation of pure NiO with 400 nm light. This is as expected because 400 nm light is below the band gap of NiO. This comparison demonstrates that the delayed transient response observed at Ni $M_{2,3}$ -edge in the heterostructure sample is a result of photoexcitation of the Fe_2O_3 layer having a smaller band gap, followed by charge transfer to the NiO layer.

We assign this spectral signature to hole transfer from Fe_2O_3 to NiO consistent with the expected band alignment for this type II heterojunction. The transient signal observed at the Ni $M_{2,3}$ -edge in the heterojunction sample shows a GSB at 65.6 eV indicating depletion of the Ni^{2+} ground state population. However, unlike the pure NiO sample, we also observe an ESA feature at 68 eV slightly higher than the Ni^{2+} GSB. This blue shift is consistent with the predicted signature for Ni^{3+} confirming that hole transfer occurs to NiO valence band states having significant Ni 3d character. Under this interpretation the temporal delay between

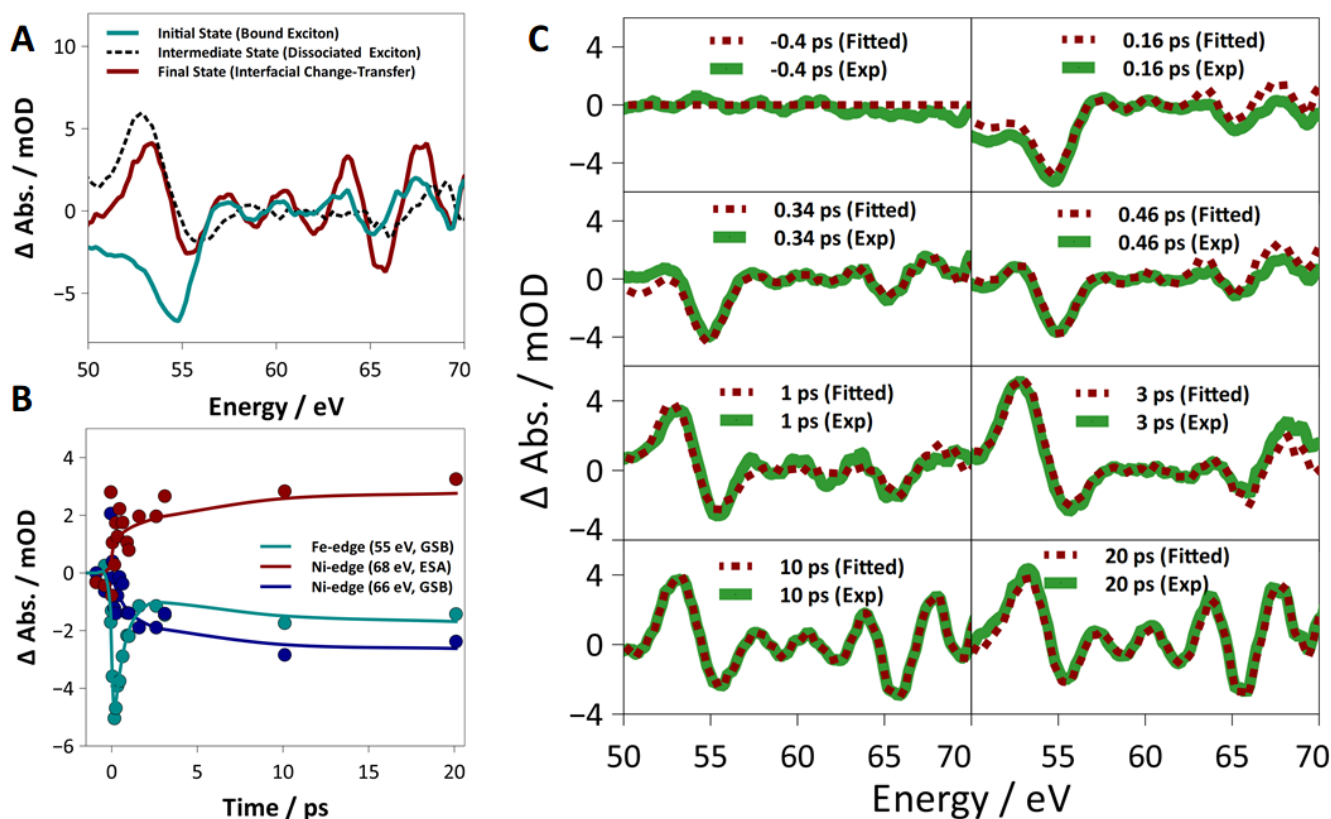


Fig. 3 (A) Vectors from the singular-value decomposition of the transient data showing the spectral signature of the bound exciton, dissociated exciton and the hole transfer state. (B) Kinetic traces for the Fe-edge GSB (cyan), Ni-edge ESA (red), and Ni-edge GSB (blue). The circles are experimental data and the solid lines represent the global fit based on a three-component, sequential kinetic model. (C) Select transient XUV-RA spectra for $\text{Fe}_2\text{O}_3/\text{NiO}$ heterojunction after photoexcitation at 400 nm depicting the spectral evolution up to 20 ps post-excitation. The red dotted traces are the reconstructed global fit traces assuming a three-component, sequential model.

transient signal measured at the Fe and Ni $M_{2,3}$ -edges represents a measure of the interfacial charge transfer rate as analyzed in detail below.

Additionally, we note the presence of a weak ESA feature in the heterojunction sample at 63.6 eV, which is also delayed in time and appears to be associated with the hole transfer process. The position of this feature closely matches the $M_{2,3}$ -absorption energy of Ni^+ at 63.2 eV.³⁷ Given the band alignment in this type II heterojunction, we were initially surprised to detect transient Ni^+ , which appears to be the result of Ni^{2+} reduction rather than oxidation. To explain this feature, we note that reduced Ni metal is often present as a defect in partially oxidized NiO.^{52,53} We confirm the presence of Ni metal defects in the samples studied here as a 1.2% contribution to the Ni 2p XPS spectrum (see Supporting Information Figure S2). Based on this observation, we hypothesize that the weak ESA feature measured at 63.2 eV arises due to hole trapping at Ni metal defect sites present at low concentrations in the NiO layer, which could explain the generation of transient Ni^+ following hole injection. The slight delay observed between the rise of Ni^{3+} signal and Ni^+ signal likely reflects the time required for hole trapping at Ni metal defect sites following injection into the NiO layer.

The second significant difference observed between Figures 2A and 2C is that the transient signal at the Fe $M_{2,3}$ -edge, which ini-

tially appears identical between these two samples, evolves quite differently for the case of the heterojunction sample compared to pure Fe_2O_3 . This can be seen most clearly in the recovery of the Fe^{3+} ground state bleach at 55 eV for the heterojunction sample. In contrast, this bleach persists for >100 ps with no sign of decay in the case of pure Fe_2O_3 .

To illustrate that the spectral evolution at the Fe $M_{2,3}$ -edge appears faster than at the Ni $M_{2,3}$ -edge, we use a three-component, sequential kinetic model to describe the spectral changes of the $\text{Fe}_2\text{O}_3/\text{NiO}$ heterojunction sample. This model assumes that an initial excited state evolves to an intermediate state with a rate constant given by k_1 , and that this intermediate then evolves to a final state with a rate constant given by k_2 . Results of the singular value decomposition of the transient data to a three-component kinetic model performed using the Glotaran software package⁵⁴ are shown in Figure 3. Figure 3A shows the three associated spectral vectors to the transient data obtained from the global fit. From the initial state to the intermediate state, spectral features significantly change at the Fe $M_{2,3}$ -edge, while only minor features are observed at the Ni $M_{2,3}$ -edge. In contrast, a significant change in the spectral signature at the Ni $M_{2,3}$ -edge and only a minor change at the Fe $M_{2,3}$ -edge are observed from the intermediate state to the final state. Given that the spectral responses at the Ni $M_{2,3}$ -edge is the result of hole transfer from Fe_2O_3 to NiO,

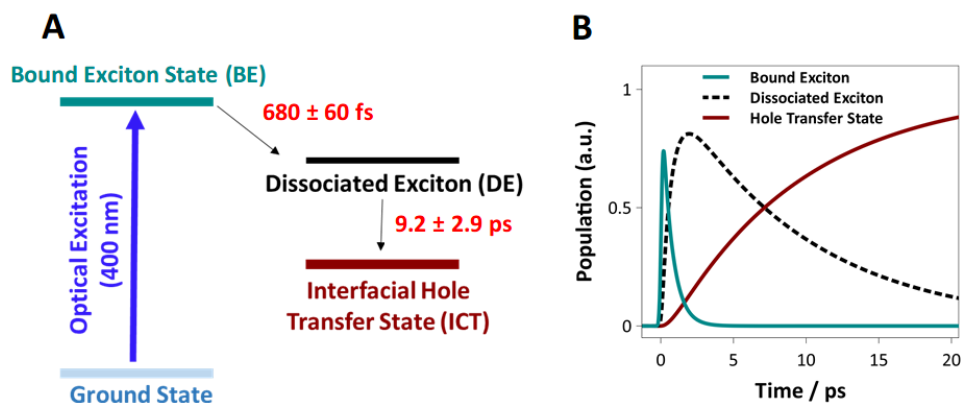


Fig. 4 (A) Schematic of the kinetic model showing the three-step, sequential kinetics for interfacial charge transfer. Photoexcitation at 400 nm produces a charge transfer exciton in Fe_2O_3 . This charge transfer exciton dissociates to form dissociated exciton with a rate constant of k_1 (680 ± 60 fs). The subsequent interfacial hole transfer across the heterojunction to NiO valence band occurs with a rate constant of k_2 (9.2 ± 2.9 ps). (B) Population of the bound exciton, dissociated exciton, and hole transfer states as obtained from the global fit using the model described in A.

we assign the final state as an interfacial charge transfer state, where a hole has migrated to the NiO layer and the electron is left in the Fe_2O_3 layer.

For comparison, a similar global analysis has also been performed on the pure Fe_2O_3 sample, and the results are reported in the Supporting Information. Comparing results for the $\text{Fe}_2\text{O}_3/\text{NiO}$ heterojunction sample and the pure Fe_2O_3 sample show that the initial excited state spectrum is nearly identical in these two systems (see Figure S5). This state has previously been assigned as a charge-transfer excited state in Fe_2O_3 . This charge-transfer state is highly localized and forms a bound exciton.³⁶ Therefore, we assign the initial state as a bound exciton state in the Fe_2O_3 layer.

Measuring the spectral evolution of this state for the pure Fe_2O_3 and the heterojunction samples shows that the Fe $M_{2,3}$ -edge evolves quite differently in these two cases. This can be seen in Figure S5 of the Supporting Information, which compares the intermediate state spectra for the heterojunction sample with that of the pure Fe_2O_3 . These spectra differ primarily in the the GSB at 55 eV, which recovers almost completely in the $\text{Fe}_2\text{O}_3/\text{NiO}$ heterojunction sample, while this feature is long-lived in Fe_2O_3 . As evidenced by the three-state spectral deconvolution, this difference at the Fe $M_{2,3}$ -edge arises at a time scale which is faster than hole transfer into the NiO overlayer. Because the presence of the NiO layer influences the Fe $M_{2,3}$ -edge kinetics at a time scale which is faster than interfacial charge transfer, we consider that this may be a result of the interfacial electric field induced in the Fe_2O_3 layer by the type II heterojunction with NiO. An estimation of the field strength at a $\text{Fe}_2\text{O}_3/\text{NiO}$ interface based on the known band alignment and estimated carrier densities is 6×10^6 V/m (see Supporting Information), and this field strength would be expected to facilitate fast exciton dissociation as described below.

Field-induced exciton dissociation has been described as a tunneling process with a rate that is proportional to the dissociation probability as given by $\exp(-E_b/edF_m)$, where E_b is exciton binding energy, e is elementary charge, d is exciton diameter, and F_m is electric field at the interface.⁵⁵ A theoretical study recently

predicted an exciton dissociation lifetime of less than 1 ps for strongly bound excitons in MoS_2 .⁵⁶ Scaling the dissociation probability by comparing E_b , F_m and d in MoS_2 and Fe_2O_3 as given in Table S2 in the Supporting information predicts a similar rate for exciton dissociation in these two systems, where a greater electric field in the monolayer MoS_2 is offset by a weaker exciton binding energy in Fe_2O_3 .

This suggests that hole transfer occurs via a case 1 mechanism, where the interfacial electric field in the space charge region leads to exciton dissociation, and charge transfer occurs by subsequent drift of the hole across the $\text{Fe}_2\text{O}_3/\text{NiO}$ interface. Consequently, we utilize the sequential, two-step kinetic model to describe this interfacial hole transfer process, where three distinct states evolve sequentially in the time domain, namely a bound exciton state (BE), a dissociated exciton state (DE), and an interfacial charge transfer state (ICT). The field driven dissociation of the BE state to the DE state occurs with a rate constant of k_1 , while the subsequent formation rate of ICT state is given by k_2 . Here k_1 and k_2 represent the rate constants for exciton dissociation and interfacial hole transfer, respectively as shown in Figure 4A. The detailed derivation of the kinetic model including convolution with the measured instrument response function is given in the Supporting Information. The fitted populations of the BE, DE, and ICT state based on the described two-step kinetic model are shown in Figure 4B. The global fit to this kinetic model shows good agreement with the experimental data as shown in Figure 3B and 3C. We find that the field driven dissociation of the BE state to DE state occurs with a time constant ($1/k_1$) of 680 ± 60 fs, while the time constant ($1/k_2$) for the formation of ICT state is 9.2 ± 2.9 ps.

This k_2 value is consistent with previous measurements of interfacial hole injection rates in other transition metal oxide and dichalcogenide systems.^{57,58} However, few experimental measurements of field-driven exciton dissociation at a semiconductor interface exist for comparison with k_1 . Attempts to estimate the exciton dissociation rate in carbon nanotubes have been made based on changes in the absorption linewidth as a function of applied electric field.¹⁴ The electric field present at the $\text{Fe}_2\text{O}_3/\text{NiO}$

interface studied here is estimated to be on the order of 6×10^6 V/m (see Supporting Information). Absorption linewidths measured at similar field strength predicts the exciton dissociation rate in carbon nanotubes to be on the order of tens to hundreds of fs. Further, the time constant of 680 ± 60 fs agrees well with predictions for sub-picosecond dissociation of strongly bound exciton in MoS₂, having a similar dissociation probability as the present system. This comparison indicates that the measured time constant for exciton dissociation in Fe₂O₃/NiO heterojunction is generally consistent with both theoretical and experimental expectations.

It is important to note that the measured k_1 time constant in this analysis represents an effective rate constant and is convoluted with all other elementary processes, which give rise to spectral evolution at the Fe M_{2,3}-edge during this same time period. Comparison with pure Fe₂O₃ shows that spectral evolution also occurs at the Fe M_{2,3}-edge during the first picosecond following photoexcitation even in the absence of a NiO heterojunction. These dynamics in the case of pure Fe₂O₃ have been studied in detail previously and are assigned as the spectral signature of small polaron formation and surface electron trapping in this material.^{34,51} Small polaron formation represents the coupling between an electronic excited state and the phonon modes of a material resulting in a lattice distortion, which stabilizes the charge transfer excited state. In the case of Fe₂O₃, this lattice distortion can be described as the expansion of the oxide lattice around the Fe²⁺ photoexcited metal center. Assuming electron density localizes on the Fe center and hole density localizes on the O ligands, this lattice expansion serves to increase the exciton bond length and facilitate fast exciton dissociation. Consequently, it is expected that electron-phonon scattering and exciton dissociation would be strongly coupled in this system.

This can be further illustrated by the following analysis. Taking the intermediate vector for pure Fe₂O₃ (see Figures S5) as the spectral signature of a small polaron state (SP), it is possible to deconvolute the Fe M_{2,3}-edge spectra of the heterojunction sample as time-evolving transient population of the BE, SP, and DE states. The amplitude coefficients associated with these states as a function of time are given in Figure S6 of the Supporting Information. From this it is possible to extract elementary rate constants for small polaron formation and exciton dissociation separately, assuming that these processes occur sequentially (i.e. small polaron formation first results in a lengthening of the exciton bond followed by dissociation). The results of fitting the BE, SP, and DE amplitude coefficients to this model, including convolution with the known instrument response, are shown as solid lines in Figure S6. These results suggest that small polaron formation occurs with a time constant of 520 ± 190 fs and that exciton dissociation occurs with a time constant of 280 ± 240 fs. This time constant for polaron formation matches within error what has been previously reported for a Fe₂O₃ surface.³⁴ The fast time constant associated with exciton dissociation indicates that given the time resolution of the present experiment, dissociation occurs almost instantly following lattice distortion, confirming that dissociation is strongly coupled to the lattice motion involved in bond elongation during the small polaron formation process.

4 Conclusion

These measurements show the ability of element specific, XUV spectroscopy to follow interfacial charge transfer in real-time and to directly probe the chemical nature of charge donor and acceptor states at semiconductor interfaces. Specifically, we identify the formation of transient Ni³⁺ within 10 ps following photoexcitation of an underlying Fe₂O₃ substrate, indicating that hole transfer occurs in this system to NiO valence band states having significant Ni 3d character. This hole injection process appears to proceed by a two-step mechanism where fast exciton dissociation occurs with an effective time constant of 680 ± 60 fs in a process which is strongly correlated with electron-phonon coupling. Exciton dissociation is followed by subsequent hole injection with a time constant of approximately 9.2 ± 2.9 ps. These results provide important insights into the chemical nature of hole acceptor states in widely used NiO charge transport layers and represent a first direct observation of exciton dynamics and charge injection at a model heterojunction interface with element-specific resolution.

5 Conflicts of interest

There are no conflicts of interest to declare.

6 Acknowledgements

This work was supported by Chemical Sciences, Geosciences and Biosciences Division, Office of Basic Energy Sciences, Office of Science, U.S. Department of Energy under DOE Grant No. DE-SC0014051.

References

- 1 M. D. Irwin, D. B. Buchholz, A. W. Hains, R. P. H. Chang and T. J. Marks, *Proc. Natl. Acad. Sci.*, 2008, **105**, 2783–2787.
- 2 J.-M. Caruge, J. E. Halpert, V. Bulović and M. G. Bawendi, *Nano Lett.*, 2006, **6**, 2991–2994.
- 3 S. Seo, I. J. Park, M. Kim, S. Lee, C. Bae, H. S. Jung, N.-G. Park, J. Y. Kim and H. Shin, *Nanoscale*, 2016, **8**, 11403–11412.
- 4 S. Liu, R. Liu, Y. Chen, S. Ho, J. H. Kim and F. So, *Chem. Mater.*, 2014, **26**, 4528–4534.
- 5 M. B. Islam, M. Yanagida, Y. Shirai, Y. Nabetani and K. Miyano, *ACS Omega*, 2017, **2**, 2291–2299.
- 6 H. Tian, B. Xu, H. Chen, E. M. Johansson and G. Boschloo, *ChemSusChem*, 2014, **7**, 2150–2153.
- 7 J.-Y. Jeng, K.-C. Chen, T.-Y. Chiang, P.-Y. Lin, T.-D. Tsai, Y.-C. Chang, T.-F. Guo, P. Chen, T.-C. Wen and Y.-J. Hsu, *Adv. Mater.*, 2014, **26**, 4107–4113.
- 8 M.-H. Li, P.-S. Shen, K.-C. Wang, T.-F. Guo and P. Chen, *J. Mater. Chem. A*, 2015, **3**, 9011–9019.
- 9 S. Mori, S. Fukuda, S. Sumikura, Y. Takeda, Y. Tamaki, E. Suzuki and T. Abe, *J. Phys. Chem. C*, 2008, **112**, 16134–16139.
- 10 M. D. Irwin, J. D. Servaites, D. B. Buchholz, B. J. Leever, J. Liu, J. D. Emery, M. Zhang, J.-H. Song, M. F. Durstock, A. J. Freeman, M. J. Bedzyk, M. C. Hersam, R. P. H. Chang, M. A. Ratner and T. J. Marks, *Chem. Mater.*, 2011, **23**, 2218–2226.

- 11 J. Yun, J. Jun, H. Yu, K. Lee, J. Ryu, J. Lee and J. Jang, *J. Mater. Chem. A*, 2017, **5**, 21750–21756.
- 12 A. Weu, T. R. Hopper, V. Lami, J. A. Kress, A. A. Bakulin and Y. Vaynzof, *Chem. Mater.*, 2018, **30**, 2660–2667.
- 13 M. Massicotte, F. Vialla, P. Schmidt, M. B. Lundeberg, S. Latini, S. Haastrup, M. Danovich, D. Davydovskaya, K. Watanabe, T. Taniguchi, V. I. Fal'ko, K. S. Thygesen, T. G. Pedersen and F. H. L. Koppens, *Nat. Commun.*, 2018, **9**, 1633.
- 14 V. Perebeinos and P. Avouris, *Nano Lett.*, 2007, **7**, 609–613.
- 15 G. Wu, Z. Li, X. Zhang and G. Lu, *J. Phys. Chem. Lett.*, 2014, **5**, 2649–2656.
- 16 M. K. P., A.-S. Sebastian, H. R. L. Z., S. Aditya, M.-R. David, M.-D. J. L. and F. R. H., *Adv. Funct. Mater.*, 2014, **24**, 3562–3570.
- 17 D. Caruso and A. Troisi, *Proc. Natl. Acad. Sci.*, 2012, **109**, 13498–13502.
- 18 D. Carsten, S. Thomas and D. Vladimír, *Adv. Mater.*, 2010, **22**, 4097–4111.
- 19 C. Wang, T. Wang, B. Wang, X. Zhou, X. Cheng, P. Sun, J. Zheng and G. Lu, *Sci. Rep.*, 2016, **6**, 26432.
- 20 E. Itoh and T. Shirotori, *Jpn. J. Appl. Phys.*, 2012, **51**, 02BK14.
- 21 D. Kawade, S. F. Chichibu and M. Sugiyama, *J. Appl. Phys.*, 2014, **116**, 163108.
- 22 J. Wu, S. Deng, N. Xu and J. Chen, *Appl. Surf. Sci.*, 2014, **292**, 454–461.
- 23 M. Chergui and E. Collet, *Chem. Rev.*, 2017, **117**, 11025–11065.
- 24 H. B. Donald, E. Pascal and W. Edgar, *J. Phys. B: At., Mol. Opt. Phys.*, 2005, **38**, S773.
- 25 D. Hayes, R. G. Hadt, J. D. Emery, A. A. Cordones, A. B. Martinson, M. L. Shelby, K. A. Fransted, P. D. Dahlberg, J. Hong, X. Zhang *et al.*, *Energy Environ. Sci.*, 2016, **9**, 3754–3769.
- 26 X. Zhang, G. Smolentsev, J. Guo, K. Attenkofer, C. Kurtz, G. Jennings, J. V. Lockard, A. B. Stickrath and L. X. Chen, *J. Phys. Chem. Lett.*, 2011, **2**, 628–632.
- 27 M. R. Harpham, S. C. Nguyen, Z. Hou, J. C. Grossman, C. B. Harris, M. W. Mara, A. B. Stickrath, Y. Kanai, A. M. Kolpak, D. Lee *et al.*, *Angew. Chem. Int. Ed.*, 2012, **51**, 7692–7696.
- 28 M. Khalil, M. A. Marcus, A. L. Smeigh, J. K. McCusker, H. H. Chong and R. W. Schoenlein, *J. Phys. Chem. A*, 2006, **110**, 38–44.
- 29 D. Kiewewetter, R. Jones, A. Camper, S. Schoun, P. Agostini and L. DiMauro, *Nat. Phys.*, 2018, **14**, 68.
- 30 E. S. Ryland, M.-F. Lin, M. A. Verkamp, K. Zhang, K. Benke, M. Carlson and J. Vura-Weis, *J. Am. Chem. Soc.*, 2018, **140**, 4691–4696.
- 31 M. Zurch, H.-T. Chang, P. M. Kraus, S. K. Cushing, L. J. Borja, A. Gandman, C. J. Kaplan, M. H. Oh, J. S. Prell, D. Prendergast, C. D. Pemmaraju, D. M. Neumark and S. R. Leone, *Struct. Dyn.*, 2017, **4**, 044029.
- 32 Y. Kobayashi, H. Timmers, M. Sabbar, S. R. Leone and D. M. Neumark, *Phys. Rev. A*, 2017, **95**, 031401.
- 33 M.-F. Lin, M. A. Verkamp, J. Leveillee, E. S. Ryland, K. Benke, K. Zhang, C. Weninger, X. Shen, R. Li, D. Fritz, U. Bergmann, X. Wang, A. Schleife and J. Vura-Weis, *J. Phys. Chem. C*, 2017, **121**, 27886–27893.
- 34 J. Husek, A. Cirri, S. Biswas and L. R. Baker, *Chem. Sci.*, 2017, **8**, 8170–8178.
- 35 S. Biswas, J. Husek and L. R. Baker, *Chem. Commun.*, 2018, **54**, 4216–4230.
- 36 S. Biswas, J. Husek, S. Londo and L. R. Baker, *Nano Lett.*, 2018, **18**, 1228–1233.
- 37 A. Cirri, J. Husek, S. Biswas and L. R. Baker, *J. Phys. Chem. C*, 2017, **121**, 15861–15869.
- 38 J. Husek, A. Cirri, S. Biswas, A. Asthagiri and L. R. Baker, *J. Phys. Chem. C*, 2018, **122**, 11300–11304.
- 39 C. J. Kaplan, P. M. Kraus, A. D. Ross, M. Zürich, S. K. Cushing, M. F. Jager, H.-T. Chang, E. M. Gullikson, D. M. Neumark and S. R. Leone, *Phys. Rev. B*, 2018, **97**, 205202.
- 40 Z. Huang, G. Natu, Z. Ji, P. Hasin and Y. Wu, *J. Phys. Chem C*, 2011, **115**, 25109–25114.
- 41 K. A. Click, B. M. Schockman, J. T. Dilenschneider, W. D. McCulloch, B. R. Garrett, Y. Yu, M. He, A. E. Curtze and Y. Wu, *J. Phys. Chem. C*, 2017, **121**, 8787–8795.
- 42 D.-Y. Cho, S. J. Song, U. K. Kim, K. M. Kim, H.-K. Lee and C. S. Hwang, *J. Mater. Chem. C*, 2013, **1**, 4334–4338.
- 43 T. J. Meyer, *Acc. Chem. Res.*, 1978, **11**, 94–100.
- 44 N. Li, D. K. Bediako, R. G. Hadt, D. Hayes, T. J. Kempa, F. von Cube, D. C. Bell, L. X. Chen and D. G. Nocera, *Proc. Natl. Acad. Sci.*, 2017, **114**, 1486–1491.
- 45 P. Olalde-Velasco, J. Jiménez-Mier, J. D. Denlinger, Z. Hussain and W. L. Yang, *Phys. Rev. B*, 2011, **83**, 241102.
- 46 J. Zaanen, G. A. Sawatzky and J. W. Allen, *Phys. Rev. Lett.*, 1985, **55**, 418–421.
- 47 C. J. Flynn, S. M. McCullough, E. Oh, L. Li, C. C. Mercado, B. H. Farnum, W. Li, C. L. Donley, W. You, A. J. Nozik, J. R. McBride, T. J. Meyer, Y. Kanai and J. F. Cahoon, *ACS Appl. Mater. Interfaces*, 2016, **8**, 4754–4761.
- 48 Q. Liu, L. Wei, S. Yuan, X. Ren, Y. Zhao, Z. Wang, M. Zhang, L. Shi, D. Li and A. Li, *RSC Adv.*, 2015, **5**, 71778–71784.
- 49 E. L. Miller and R. E. Rocheleau, *J. Electrochem. Soc.*, 1997, **144**, 3072–3077.
- 50 J. Vura-Weis, C.-M. Jiang, C. Liu, H. Gao, J. M. Lucas, F. M. F. de Groot, P. Yang, A. P. Alivisatos and S. R. Leone, *J. Phys. Chem. Lett.*, 2013, **4**, 3667–3671.
- 51 L. M. Carneiro, S. K. Cushing, C. Liu, Y. Su, P. Yang, A. P. Alivisatos and S. R. Leone, *Nat. Mater.*, 2017, **16**, 819.
- 52 S. Biswas, J. Husek, S. Londo and L. R. Baker, *J. Phys. Chem. Lett.*, 2018, **9**, 5047–5054.
- 53 A. P. Grosvenor, M. C. Biesinger, R. S. C. Smart and N. S. McIntyre, *Surf. Sci.*, 2006, **600**, 1771–1779.
- 54 J. Snellenburg, S. Laptinok, R. Seger, K. Mullen and I. Van Stokkum, *J. Stat. Softw.*, 2012, **49**, 1–22.
- 55 M. Massicotte, F. Vialla, P. Schmidt, M. B. Lundeberg, S. Latini, S. Haastrup, M. Danovich, D. Davydovskaya, K. Watanabe, T. Taniguchi *et al.*, *Nat. Commun.*, 2018, **9**, 1633.
- 56 S. Haastrup, S. Latini, K. Bolotin and K. S. Thygesen, *arXiv preprint arXiv:1602.04044*, 2016.

- 57 X. Yang and N. Tamai, *Phys. Chem. Chem. Phys.*, 2001, **3**, 3393–3398.
- 58 S. B. Homan, V. K. Sangwan, I. Balla, H. Bergeron, E. A. Weiss and M. C. Hersam, *Nano Lett.*, 2017, **17**, 164–169.